ENGINE LES WITH FUEL-SPRAY MODELING

Mateus Dias Ribeiro ✉

Maurício Araújo Zanardi

José Antônio Perrella Balestieri

Faculdade de Engenharia de Guaratinguetá, UNESP

E-mail: mateusdiasbr@gmail.com

Peter Janas

Chair of Fluid Dynamics, University of Duisburg-Essen

Rafael Aguera Rezeno da Silva

Alex de Souza Rodrigues

ThyssenKrupp Metalúrgica Campo Limpo

Abstract: *Direct injection spark ignition (DISI) engines aim to reduce the specific fuel consumption, while respecting the strict emission standards for internal combustion engines. The development of models to correctly describe the physical phenomena related to the injection of fuel sprays in engine combustion chambers became more relevant over the last years. In this work, large eddy simulations (LES) of the "Spray G" multi-hole gasoline injection test case provided by the ECN (Engine Combustion Network) were performed. Special attention was given to the phenomena of momentum exchange, droplet breakup, evaporation and an Eulerian-Lagrangian method was used to couple the discrete medium (spray particles) with the continuous medium (gas phase). The Reitz-Diwakar model was employed for the droplet breakup and the Ranz-Marshall model for the heat transfer between liquid and gas phase. The penetration length of the spray jet obtained by LES was validated against experiments and good agreement was observed.*

Keywords: *Fuel-Spray, Internal Combustion Engine, LES, Lagrangian, OpenFOAM*

1 INTRODUCTION

Today's pollutant regulations aim to reduce greenhouse gases and pollutant emissions of internal combustion engines. European CO_2 emission projections are targeting at an extremely low fleet average of 95 g/km in 2021 for all new cars (The International Council on Clean Transportation (2014)). This brings to discussion the development of technologies to improve efficiency and combustion quality of next generation engines, from which stratified-charge combustion can be highlighted.

Stratified-charge combustion can be achieved in engines by injecting the fuel directly into the combustion chamber, which interacts with the hot gases inside the combustion chamber. Careful studies on spray, droplet evaporation, breakup and mixture processes are necessary to develop detailed numerical models and experimental configurations to allow a change from the standard port-fuel injection to the modern state of art DI engines. These engines have the potential to decrease the specific fuel consumption under engine part load conditions by means of stratified-charge combustion. Furthermore, Baumgarten (2005) has pointed out that load throttling can be eliminated under part load and thus pumping losses are minimized. The evaporation of fuel droplets inside the chamber cools down the charge, which allows to increase the compression ratio compared to conventional spark ignition engines. Especially during part load and full load the thermal efficiency will be increased. In full load conditions, however, stratified combustion is no longer capable to achieve maximum torque since turbulence becomes too strong to allow a compact and ignitable mixture cloud next to the spark-plug. Cycle-to-cycle variations may also perturb the spray jet and impact the mixture formation, as shown in Goryntsev et al. (2010). Thus, the engine must operate under homogeneous stoichiometric or even fuel-rich mixture conditions to deliver the necessary amount of energy. This is done by early injection during the intake stroke and conventional throttle load.

To deal with the transition period between part load and full load conditions, a two-stage injection was sought. This approach combines early injection during the intake stroke and late injection during compression, creating a dual zone mixture in the chamber. According to the work of Yang & Anderson (1998) this approach can be considered as a good alternative to DI engines by combining the volumetric efficiency improvement achieved by the early injection and the suppression of knocking tendency of the late injection. Zheng, Tian, & Zhang (2015) studied the influence of split injection proportion and timing for the early injection on a turbocharged gasoline direct-injection (GDI) engine. According to the authors, 25%-75% proportion for late and early injections, respectively, could be a reasonable configuration for low speed (1200 rpm) operation, due to the formation of a local, ignitable and rich mixture around the spark plug leading to higher thermal efficiency and low soot emissions. They also stated that an advancement of the second injection lead to an decreasing of NO_x and particulates, because more time for evaporation and mixing is available.

Furthermore, Liu et al. (2015) evaluated particulate and fuel economy improvement by the use of dual-fuel approach (gasoline and methanol) in a DISI engine and found out that the break specific fuel consumption could be improved up to 22% with a reduction of particulates by 99.6% in comparison with a pure gasoline DI under same conditions (CR: 14:1, stoichiometric, full load). Kim, Cho, & Min (2015) reported the same trend for particulate and fuel consumption, but detected an increase in Nitrogen Monoxide (NO_x) and Total Hydrocarbon (THC) for a similar engine conditions. Additionally to emissions and consumption benefits, a

dual-fuel strategy could extend the high load limit of the engines by reducing the knocking tendency, as reported by Liu, Wang, & Wang (2015). Maricq, Szente, & Jahr (2012) point out that significant benefits to particulate emissions could only be achieved with blends containing more than 30 vol$\%$ in ethanol for a turbocharged DISI engine passenger car. However, Karavalakis et al. (2015) reported that even medium or low (10-20$\%$) ethanol and iso-butanol blends could achieve reasonable reductions of THC and Non-Methane Hydrocarbons (NMHC).

Regarding the specific and detailed modeling of fuel-sprays in high pressure combustion chambers, a large amount of work can be found in the literature. Vuorinen et al. (2011) perfomed large-eddy simulations (LES) of a Diesel spray, by a LPT approach with the open-source code OpenFOAM. They pointed out that the spray droplet size affects the mixing process and that attention should be paid on the breakup model, since many models neglect important phenomena like resonance breakup for low speed particles. A good literature review on the use of LPT methods for spray modeling can be found in Subramaniam (2013), with focus on the Lagrangian-Eulerian (LE) approach, in which the spray droplets are modeled with LPT and the gaseous phase. Lucchini, D'Errico, & Ettorre (2011) applied a Reynolds-Averaged Navier Stokes (RANS) model together with LPT to simulate a Diesel spray under engine-like-conditions. Jangi et al. (2015) performed simulations of a diesel spray test case and validated the results against experimental data, using the LE approach with OpenFOAM.

The aim of the present work is to make further contributions to the field of stratified-charge combustion in internal combustion engines by means of a preliminary study of the "Spray G" test-case provided by the Engine Combustion Network (ECN).

1.1 Basic breakup concepts of liquid droplets

Different mechanisms exist to produce spray droplets from a round continuous liquid jet. Reitz & Bracco (1986) distinguished between four different breakup regimes, the Rayleigh regime, the first and second wind-induced regimes and the atomization regime. After the primary breakup, the spray-jet particles are subject to secondary breakup, they continue breaking up into even smaller particles, which can be further categorized. Baumgarten (2005) distinguishes among five different liquid drop breakup regimes: vibrational breakup (1), bag breakup (2), bag / streamer breakup (3), stripping breakup (4) and catastrophic breakup (5). Figure 1 illustrates the five breakup regimes according to ibid.

The relative velocity between the liquid/gas interface induces aerodynamic forces that create oscillations in the droplet surface. The growing of the amplitude of these oscillations results on droplet breakup. The gas phase Weber number $\mathrm{We_g} = \mathrm{u^2_{rel}} \mathrm{D} \rho_\mathrm{g} / \sigma$ is the relevant parameter for the mechanism of liquid drop breakup. This number is a relation between the aerodynamic force, which tends to break up droplets into smaller particles and the surface tension force, which on the other hand tries to keep the parent droplets in their spherical shape. The $\mathrm{u^2_{rel}}$ is the relative velocity between particle and gas, D is the particle diameter, ρ_g is the gas density and σ is the droplet surface tension.As the droplets become smaller, the surface tension necessary to break it up becomes bigger and therefore the relative velocity must also be bigger to disintegrate the drop.

Experimental investigations show that distinct breakup regimes can be divided according to a range of Weber numbers. Table 1 presents the transition Weber numbers for different breakup regimes. Regarding the numerical simulation of secondary breakup processes, several models

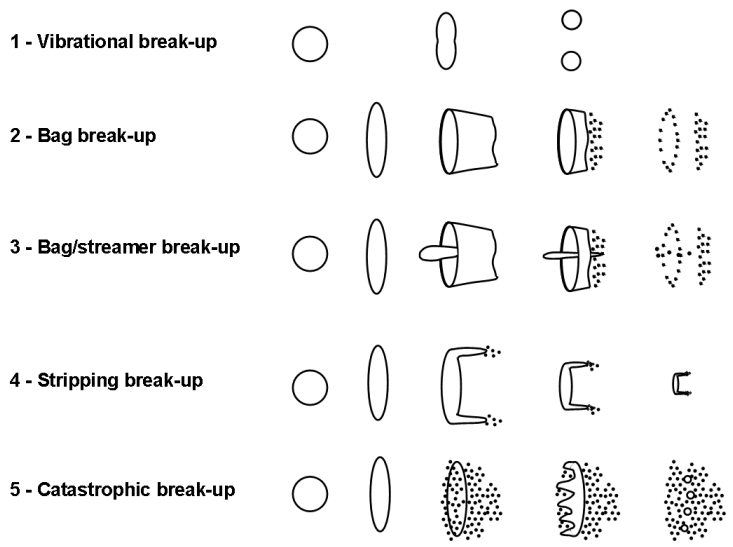

Figure 1: Droplet breakup according to Wierzba (1990)

have been proposed in the literature. The Reitz-Diwakar model was chosen in this work and will be described in subsection 2.1.2.

Table 1: Transition Weber numbers for different regimes as in Baumgarten (2005)

Wierzba	Weber number	Arcoumanis et al.	Weber number
1. Vibrational	≈ 12	1. Vibrational	≈ 12
2. Bag	< 20	2. Bag	< 18
3. Bag-streamer	< 50	3. Bag	< 45
4. Stripping	< 100	4. Chaotic breakup	< 100
5. Catastrophic	> 100	5. Sheet stripping	< 350
		6. Wave crest stripping	< 1000
		7. Catastrophic	> 1000

1.2 Full-cone sprays

Figure 2 shows a schematic representation of a full-cone spray, which is also the objective of the here presented study. In passenger cars, the injection hole may be smaller than 1 mm and the injection pressure can vary from 100-200 bar to several 1000 bars in Diesel engines.

Primary breakup happens just after the injection hole exit and forms the first droplets, which are then exposed to secondary breakup further downstream due to aerodynamical forces. The spray cloud forms a spray cone angle Φ, which is usually given as input parameter in numerical models. A random distribution of particles (measured or assumed by a probability density function) can be then imposed within the angle of the spray as boundary condition. As fuel

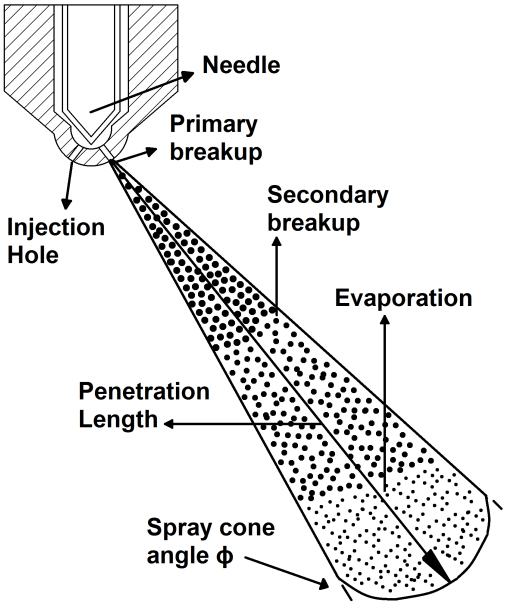

Figure 2: Schematic representation of a full-cone spray

travels further into the gaseous medium, it changes heat with the gas phase, evaporates and mixes with the combustion chamber charge.

In the study of fuel sprays, it is important to define the spray penetration length, which is here denoted as the distance from the injection hole to the spray tip. However, different definitions for the penetration length can be found in the literature, as shown in Hiroyasu & Arai (1990) and Dent (1971). Equation (1) presents the penetration length of a spray injected in a hot combustion chamber as proposed by Dent:

$$S = 3.07\left(\frac{\Delta p}{\rho_g}\right)^{0.25}(tD)^{0.5}\left(\frac{294}{T_g}\right)^{0.25} \tag{1}$$

In this equation, $\Delta \mathrm{p}$ is the difference between the injection pressure and the combustion chamber pressure, ρ_{g} is the density of the gas phase, t is the time, D is the nozzle diameter and $\mathrm{T_g}$ is the gas temperature. A correlation for the spray cone angle has been provided by Heywood (1988), which is given in Eq. (2).

$$tan\left(\frac{\phi}{2}\right) = \frac{4\pi}{3 + 0.28(L/D)}\left(\frac{\rho_g}{\rho_l}\right)^{0.5} f(\gamma) \tag{2a}$$

$$f(\gamma) = \frac{\sqrt{3}}{6}(1 - e^{-10\gamma}), \gamma = \left(\frac{Re_l}{We_l}\right)^2 \frac{\rho_l}{\rho_g} \tag{2b}$$

In these equations, ρ_{l} is the density of the liquid phase. The (L/D) relation is a parameter related to the nozzle geometry, $\mathrm{Re_l}$ is the Reynolds number of the liquid droplets and $\mathrm{We_l}$ the liquid Weber number.

2 SPRAY MODELING

2.1 Modeling of the gas phase

An Euler-Lagrange approach is used for the description of the gas phase and the fuel droplets. The large scales of the given flow must be separated from the small scales by applying a filter in space and in time. Scales larger than the filter size are directly solved, while the others are modeled. The unresolved subgrid scales are modeled by the standard Smagorinsky model. For dealing with compressible flows, a change of variable is often applied for every quantity of interest φ, in which φ is density-weighted by the operation $\overline{\rho}\tilde{\varphi} = \overline{\rho\varphi}$. This is known as Favre-filtering and results in the Favre-filtered variable $\tilde{\varphi}$.

In order to account for the presence of Lagrangian particles, source terms (S_ρ for mass, $\mathrm{S_u}$ for momentum and $\mathrm{S_h}$ for entalphy) must be added to the governing equations. The Favre-filtered governing equations read for balance of mass in Eq. (3), balance of momentum in Eq. (4) and balance of total energy in Eq. (5):

$$\frac{\partial\bar{\rho}}{\partial t} + \frac{\partial(\bar{\rho}\tilde{u_j})}{\partial x_j} = S_\rho \tag{3}$$

$$\begin{aligned} &\frac{\partial(\bar{\rho}\tilde{u_i})}{\partial t} + \frac{\partial(\bar{\rho}\tilde{u_i}\tilde{u_j})}{\partial x_j} = \\ &\frac{\partial}{\partial x_j}\left[\bar{\rho}\bar{\nu}\left(\frac{\partial\tilde{u_j}}{\partial x_i} + \frac{\partial\tilde{u_i}}{\partial x_j}\right) - \frac{2}{3}\bar{\rho}\bar{\nu}\frac{\partial\tilde{u_k}}{\partial x_k}\delta_{ij} - \bar{\rho}{\tau_{ij}}^{sgs}\right] - \frac{\partial\bar{p}}{\partial x_i} + \bar{\rho}g_i + S_u \end{aligned} \tag{4}$$

$$\frac{\partial(\bar{\rho}\tilde{h})}{\partial t} + \frac{\partial(\bar{\rho}\tilde{h}\tilde{u_j})}{\partial x_j} + \frac{\partial(\bar{\rho}\tilde{K})}{\partial t} + \frac{\partial(\bar{\rho}\tilde{K}\tilde{u_j})}{\partial x_j} = \frac{\partial}{\partial x_j}\left(\alpha_{eff}\frac{\partial\tilde{h}}{\partial x_j}\right) + \frac{\partial\bar{p}}{\partial t} + S_h \tag{5}$$

For the mass fraction of the involved species, Eq. (6) is solved and reads:

$$\frac{\partial(\bar{\rho}\tilde{Y_i})}{\partial t} + \frac{\partial(\bar{\rho}\tilde{Y_i}\tilde{u_j})}{\partial x_j} = \frac{\partial}{\partial x_j}\left(\mu_{eff}\frac{\partial\tilde{h}}{\partial x_j}\right) + S_{Y_i} \tag{6}$$

The additional transport equation for $\mathrm{Y_i}$ in (6) features a source term $\mathrm{S_{Y_i}}$, so that the mass fraction of each species can be updated as long the particles are being evaporated.

2.1.1 Particle phase

In this work the parcel approach is used to reduce the computational effort. A spray is composed of a large number of particles of different diameters and handling each one of them would be very computational demanding. In order to circumvent the problem of simulating each particle separately, one can define a parcel as a group of droplets with the same properties,

thus only bins of particles need to be treated numerically. Another reasonable assumption is to consider that all particles are perfectly spherical, having a diameter d.

The size distribution of the injected droplets is modeled by the cumulative probability density function (CDF) Rosin-Rammer as shown in Eq. (7):

$$F(x, n, d) = 1 - e^{-(x/d)^n} \tag{7}$$

In this work, it was assumed that n = 3 and the maximum and minimum droplet diameters were defined as 100 μm and 1.5 μm, respectively.

Due to the secondary breakup, spray droplets feature a non-uniform distribution of diameters and thus the calculation of an average of the particle size is relevant. For this, the Sauter mean diameter (SMD or d_{32}) in Eq. (8) is employed, defined as the diameter of a modeled sphere that has the same volume/surface area ratio to the sum of all droplet volumes divided by the sum of all droplet surface areas in the spray cloud.

$$\frac{V_m}{A_m} = \frac{\sum_{i=1}^{n} \frac{4}{3}\pi(d_p/2)^3}{\sum_{i=1}^{n} 4\pi(d_p/2)^2} = \frac{\sum_{i=1}^{n}(d_p/2)^3}{\sum_{i=1}^{n} 3(d_p/2)^2} = \frac{d_{32}}{6} \tag{8a}$$

$$d_{32} = 6\frac{V_m}{A_m} \tag{8b}$$

$\mathrm{V_m}$ and $\mathrm{A_m}$ are the volume and surface areas of the modeled sphere, while $\mathrm{d_p}$ is the diameter of each droplet and d_{32} the sauter mean diameter.

The velocity injection is specified providing the mass flow rate and the discharge coefficient of the injection hole, as in Eq. (9):

$$U_{inj} = \frac{\dot{m}}{\rho C_{dis} A} \tag{9}$$

In Eq. (9), $\dot{\mathrm{m}}$ is mass flow rate profile, ρ the fluid density, A the hole cross section and $\mathrm{C_{dis}}$ is the discharge coefficient. The discharge coefficient is defined as the ratio of the actual and theoretical discharge delivered by a nozzle.

Finally, for a complete description of the spray cone, one has also to define the direction of the injected velocity for each parcel, so that the parcels are injected over a predefined range. For this, the expression in Eq. (10) is used:

$$\alpha = \frac{d - d_{max}}{d_{min} - d_{max}}\alpha_{max} \tag{10}$$

In Eq. (10), α_{max} is the maximum injection allowed angle, $\mathrm{d_{max}}$ is the maximum parcel diameter and $\mathrm{d_{min}}$ is the minimum parcel diameter. Thus, the smaller parcels are injected within an angle, while the larger ones go straight.

When liquid fuel particles are injected at high velocities in a quiescent gas environment, they are decelerated by the gaseous environment. The exchange of momentum between liquid and gas phase takes place due to the relative velocity between them. The equation Eq. (11), as shown by Vuorinen et al. (2011), denotes this exchange of momentum by evaluating the resulting drag force over a liquid parcel moving with relative velocity $\mathrm{u_{res}}$ with respect to the gas phase.

$$\frac{1}{6}\rho_P \pi d^3 \frac{du_P}{dt} = \frac{1}{2}(u_g - u_P)|u_g - u_P|\rho_g C_D \frac{\pi d^2}{4} \tag{11}$$

The term on the left side in Eq. (11) represents the change of the acceleration of the liquid fuel particle, while the term on the right side denotes the drag force due to its relative motion to the gas phase. The subscript g refers to the gas phase and P to the liquid parcel of diameter d.

The drag coefficient $\mathrm{C_D}$ is calculated assuming spherical particles and is calculated using the Reynolds number of the gas phase $\mathrm{Re_g} = \mathrm{du_{rel}}\rho_\mathrm{g}/\mu_\mathrm{g}$. The correlation for evaluating $\mathrm{C_D}$ is presented in Eq. (12).

$$C_D = \begin{array}{r} \dfrac{24}{Re_g}\left(1 + \dfrac{1}{6}{Re_g}^{2/3}\right), Re \leq 1000 \\ 0.424, Re > 1000 \end{array} \tag{12}$$

Finally, the parcels can be tracked by updating their positions according to Eq. (13).

$$\frac{dx_P}{dt} = u_P \tag{13}$$

As soon as the liquid particles get into the domain, besides exchanging momentum, they also exchange heat with the gas phase. The liquid phase exchanges heat with the gas due to diffusive and convective transport and radiation. The heat exchange increases the temperature until the particle reaches the boiling temperature and evaporates. This is very important for the mixing process, combustion and formation of pollutants since the fuel starts to burn only when it is in the vapor phase.

In addition to the assumption of perfect spherical particles, one may also neglect the effect of radiation, since it is small compared to the convection. Furthermore, the evaporation modeling is based on the averaged flow field around the particles, because the flow among them is not feasible to be calculated.

Baumgarten (2005) obtains the following energy balance for a liquid particle, presented in Eq. (14):

$$m_P c_{p,l} \frac{dT_P}{dt} + \Delta h_{evap} \frac{dm_{evap}}{dt} = \lambda_g \pi d_P (T_\infty - T_P) \frac{\zeta}{e^\zeta - 1} Nu \tag{14}$$

The terms Nu and ζ are shown in Eq. (15) and Eq. (16), respectively.

$$Nu = \frac{\alpha d_P}{\lambda_g} \tag{15}$$

$$\zeta = \frac{\dot{m}_{evap} c_{p,vap}}{Nu \lambda_g \pi d_P} \tag{16}$$

Where T_∞ is the temperature of the gas phase and $\mathrm{T_P}$ is the temperature of the parcel, $\mathrm{d_P}$ is the parcel diameter, λ_g is the thermal diffusivity of the gas mixture, Nu is the Nusselt number and ζ is a dimensionless correction factor accounting of the reduced heat transfer due to the simultaneous mass transfer from the parcel to the gas phase. In Eq. (14), the first term represents the energy necessary to heat up the liquid fuel parcel until a given temperature in an interval dt, where $\mathrm{m_p}$ is the mass of the parcel, $\mathrm{T_P}$ its temperature and $\mathrm{c_{p,l}}$ the specific heat at constant pressure of the liquid fuel. The second term accounts for the energy necessary to evaporate the parcel mass $\mathrm{m_{evap}}$ during the interval dt. The term on the right hand side accounts to the heat transfer between the liquid and gas phase.

The appropriate Nusselt number, that accounts for the relative velocity between the particle and gas was proposed by Marshall & Ranz (1952) and reads in Eq. (17):

$$Nu = 2.0 + 0.6 Re^{1/2} Pr^{1/3} \tag{17}$$

In this equation, the Reynolds number is denoted as Re and the Prantdl number as Pr, which are calculated with the properties of the gas phase.

2.1.2 Breakup model

The breakup model used in the present work is the Reitz-Diwakar model, which works according to two assumptions. First, atomization and drop breakup near the nozzle within the spray cloud are considered to be indistinguishable, thus the blob method is used to represent the jet breakup into the first spray droplets. By using this method, a detailed simulation of the phenomena near the nozzle is replaced by the injection of big spherical droplets, which have a uniform diameter, similar to the nozzle hole size. The speed of these first droplets is determined by the previously presented Eq. (9), and their direction by Eq. (10). The injected big droplets are then subject to secondary breakup as they travel through the gaseous medium. Equation 18 shows how $\mathrm{We_P}$ is calculated, where ρ_l and $\mathrm{D_P}$ are the density and diameter of the liquid parcel, $\mathrm{u_{rel}}$ is the relative velocity to the gas phase and σ is the surface tension.

$$We_P = \frac{\rho_l {u_{rel}}^2 D_P}{\sigma} \tag{18}$$

The second assumption is related to the secondary breakup. The Reitz-Diwakar model distinguishes between two droplet breakup regimes, which are the bag breakup and the stripping

breakup. These regimes were illustrated in Fig. 1. The bag breakup occurs when $\mathrm{We_P}$ (Weber number of a liquid parcel) is greater than a certain critical value ($\mathrm{We_P} > \mathrm{We_{crit}}$). In this breakup regime, the parent particle is firstly stretched perpendicularly to its direction until a given size, then aerodynamical forces start acting over the droplet surface parallel to its direction. Since the surface tension acts against these forces, the particle takes the form of a bag with a very thin surface. As the particle continues its movement, the surface tension becomes too weak to support the strength of the aerodynamical forces and the particle breaks up into several product droplets, with much smaller diameter. The characteristic breakup time in this regime is giving by Eq. 19 and the new stable particle radius after breakup is shown in Eq. 20. The time factor $\mathrm{C_1}$ for bag breakup is assumed to be 0.785 and $\mathrm{We_{crit}}$ is 6.

$$t_{br} = C_1 \sqrt{\frac{\rho_P {r_P}^3}{2\sigma}} \tag{19}$$

$$r_{stable} = \frac{6\sigma}{\rho_g {u_{rel}}^2} C_1 \tag{20}$$

Independent on the breakup regime, the reduction of the particle radius is described by Eq. 21:

$$\frac{dr_P}{dt} = \frac{-(r_P - r_{stable})}{t_{br}} \tag{21}$$

In Eq. 21, $\mathrm{r_p}$ is the particle radius, $\mathrm{r_{stable}}$ the new stable radius of the particle after breakup and $\mathrm{t_{br}}$ is the characteristic breakup time. The parameters $\mathrm{r_{stable}}$ and $\mathrm{t_{br}}$ are calculated according to the breakup regime, as it will be presented below.

If $\mathrm{We_P}/\sqrt{\mathrm{Re}} > \mathrm{C_{s1}}$, stripping breakup will occur. The constant C_{s1} is the Weber number factor for stripping and has the value 0.5. In this regime, the parent droplet is also firstly stretched to a given size. Then, due to the high aerodynamical forces, product droplets of very small diameters are stripped from the parent one. The size of the parent particle is then continuously reduced until at the end only smaller particles are present. The characteristic breakup time in this regime is giving by Eq. 22 and the new stable particle radius after breakup can be calculated with Eq. 23.

$$t_{br} = C_2 \frac{r}{u_{rel}} \sqrt{\frac{\rho_P}{\rho_g}} \tag{22}$$

$$r_{stable} = \frac{\sigma^2}{2{\rho_g}^2 {u_{rel}}^3 \nu} \tag{23}$$

2.1.3 Numerical setup

The open-source tool box OpenFOAM in the version 2.3.x, was chosen for the spray simulations. The computational domain of the spray simulation is a box with dimensions 70 mm in x-direction, 70 mm in y-direction and 60 mm in z (spray cloud axial axis). The grid has equidistant hexahedral cells with a resolution of 0.5 mm, which gives a total of 2.35 million cell elements. To avoid stability problems induced by the high velocities present at the injector nozzle, total diminishing varation (TVD) schemes were used for the solution of the convective terms of the governing equations. The implicit second-order backward scheme was used for the time integration and the standard Smagorinsky ($\mathrm{C_S} = 0.062$) LES (large-eddy simulation) model was employed for the turbulence. Finally, adjustable time step was set to a maximum CFL number of 0.1. The duration of the spray simulation was of approximately one day, using 96 CPUs provided by the Chair of Fluid Dynamics from the University of Duisburg-Essen.

2.2 Test-case: ECN "Spray G"

The test-case chosen to validate this work is the "Spray G" from ECN (Engine Combustion Network), where a multi-hole gasoline spray injection system was used. The operating conditions are summarized in Table 2 and Fig. 3 illustrates the spray cloud formed during the injection. Some experimental and modeling data is available for this test-case, which is used for the validation of the present model. As this test-case is quite new, most data is not published yet, thus not available for comparison.

Table 2: "Spray G" ECN (2015)

Fuel	Iso-octane
Injection pressure	20 MPa
Fuel temperature	90 $^{\circ}\mathrm{C}$ (363 K)
Ambient temperature	300 $^{\circ}\mathrm{C}$ (573 K)
Ambient density	3.5 $\mathrm{kg/m^3}$
Ambient pressure	6 bar (600 kPa)
Ambient composition	89.71% $\mathrm{N_2}$, 6.52% $\mathrm{CO_2}$, 3.77% $\mathrm{H_2O}$
Injected quantity	10 mg
Injection duration	780 μs
Number of nozzle holes	8 (equally spaced)
Hole diameter	165 μm
Fully included angle	80°

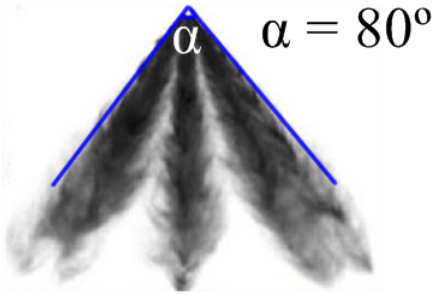

Figure 3: "Spray G" ECN (2015)

3 RESULTS AND DISCUSSION

Figure 4 shows how the spray penetration length is defined and the locations where the iso-octane mixture fraction and temperature values are taken, as well the spray.

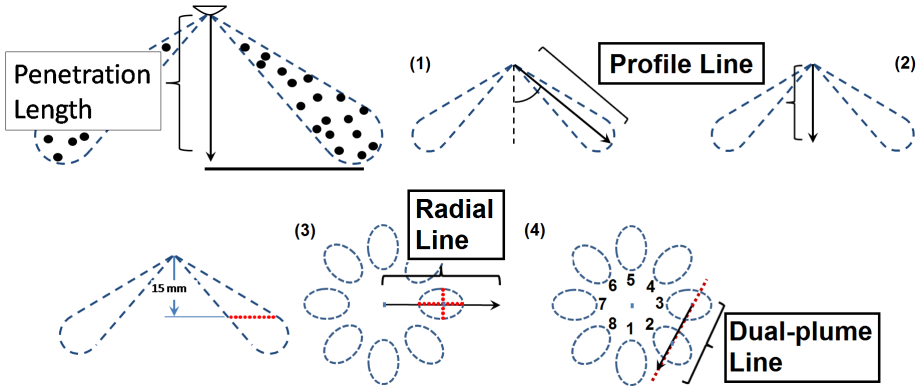

Figure 4: Definition of penetration length and planes (adapted from ECN workshop)

Figure 5 presents the vapour penetration length curve obtained by the LES simulation in comparison to the vapour and liquid penetration length curves obtained by the experiments. The penetration length curves show that at the beginning the simulation under predicts the experiment. At approximately 500 μs ASOI (after start of injection), the vapour penetration length in the simulation hits the experimental value and since then its value is slightly over predicted.

The under prediction at the beginning can be explained by the model assumption of uniform distribution of particles within the spray jet angle of 25°. In reality, this distribution is not uniform and more particles are concentrated in the middle of the jet. The over concentration in the middle makes the jet to flow faster and deeper as in the case with uniform distribution. The over prediction after a certain time may be explained by the use of a TVD numerical scheme for the solution of the momentum equation. Although it brings the advantage of good stability, the use of TVD schemes with LES can lead to strong dissipation of the present turbulent scales. The presence of only relative large scales observed by flow visualizations (Fig. 6) is evidence that too much dissipation is taking place. Besides, the mesh grid size of 0.5 mm still may be too coarse to represent the physics of the phenomenon correctly.

In Fig. 6, the full-spray (eight jets) are shown for instants 0.6 ms and 1.4 ms after start of injection. In (a), spray droplets are plotted colored by size. In (b), the gas-phase velocity

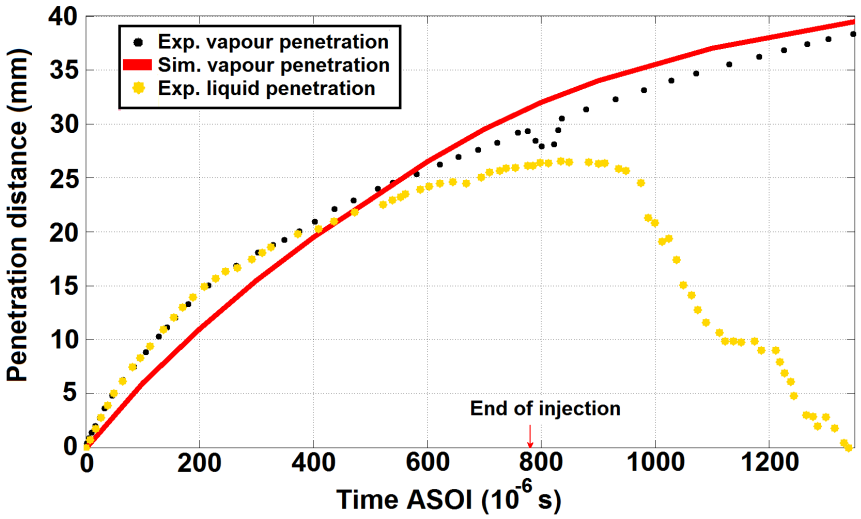

Figure 5: Penetration length (Simulation vs. Experiments)

vector plot is shown at a plane over spray plumes 1 and 5. In (c) and (d), the iso-octane mixture fraction and the gas-phase temperature plots are shown in a transparent plane over spray plumes 1 and 5, so that spray plumes 2, 3 and 4 can also be seen (see Fig. 4 for spray plumes orientation and numbering).

From the start of the injection, the number of parcels inside the domain increases linearly with time until end of the injection. After this, the number of parcels starts to decrease as long the parcels evaporate. When the number of parcels reaches zero, it means that the entire liquid fuel mass was already transferred to the gas phase. In Fig. 7 (a), the number of parcels vs. time is plotted. In Fig. 7 (b), the maximum parcel diameter and the Sauter-mean diameter are shown. The maximum diameter of the particles during the injection duration (from 0 until 780 μs) varies around the value of 100 μm, which is also the maximum diameter used in the Rosin-Rammler distribution. Just after injection start, the SMD is about 60 μm, decreasing very fast to something bigger than 20 μm and then due to the breakup and evaporation processes, the maximal diameter size decreases abruptly until 45 μm at 900 μs. Since then the parcels continue reducing their diameters until no more particles are represented.

Figure 8 shows the iso-octane mixture fraction and temperature of the gaseous phase curves at 0.6 ms after the start of injection along the jet axis. The initial temperature inside the domain is 573 K and the fuel is injected with a temperature of 363 K. As long the fuel penetrates into the domain, the temperature inside it decrease, because heat is exchanged between fuel droplets and gas. As one can observe, higher iso-octane mixture fraction values are more likely to be found at the spray jet tip, because particles at that spot are smaller due to breakup and hence evaporate faster.

Results along the z-axial direction, starting from the injector tip, are shown in Fig. 9. At 0.6 ms after start of injection, high mixture fraction and low temperature values are found a few millimeters downstream from the injector nozzle, due to influence of the formed spray cloud. This influence is diminished further downstream, since each jet makes an angle of 40° with the axial direction.

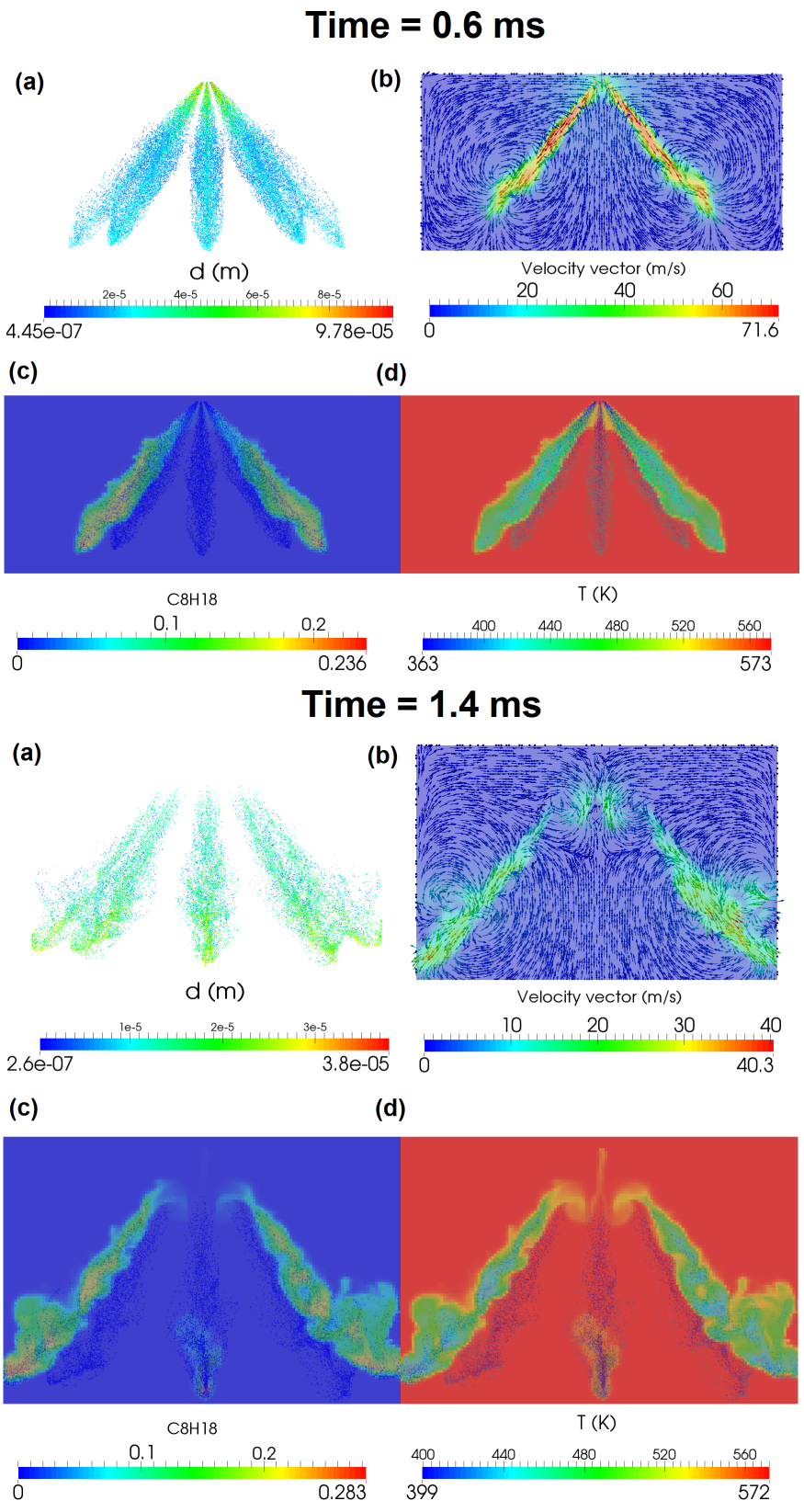

Figure 6: Simulation at 0.6 ms and 1.4 ms (liquid droplets colored by size (a), gas-phase velocity-vector plot (b), iso-octane mixture fraction plot (c), gas-phase temperature plot (d))

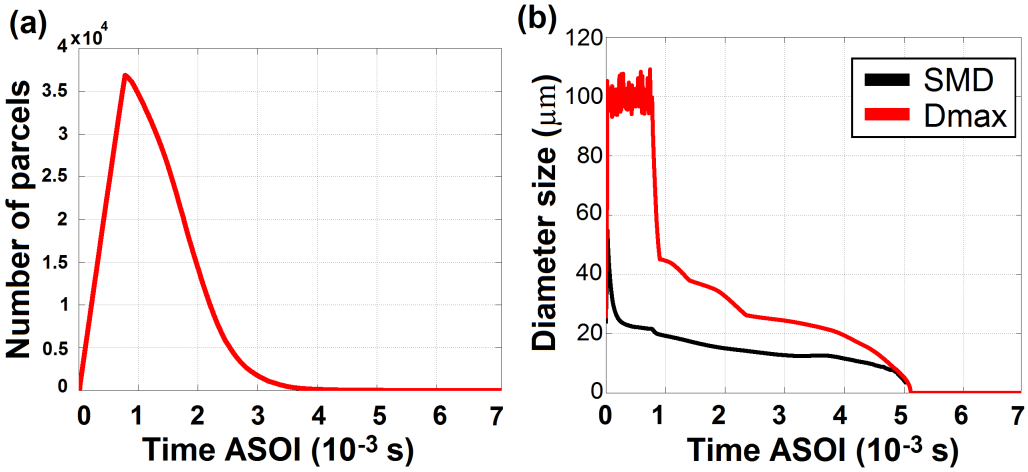

Figure 7: SMD and maximum diameter vs. time

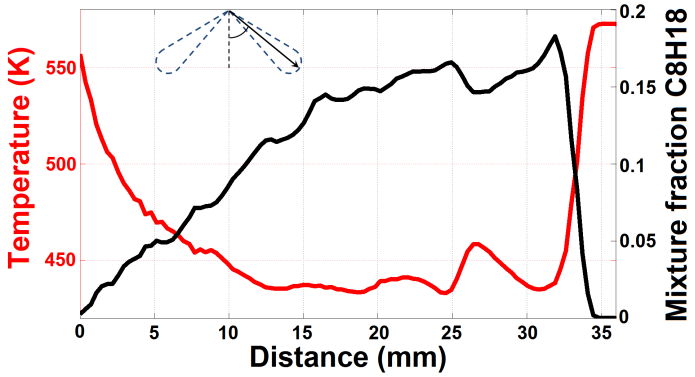

Figure 8: Temperature (red) and Iso-octane mixture fraction (black) at 0.6 ms (I)

Results on cross-section planes at 15 mm downstream from the injector nozzle are shown in Fig. 10, in which the values are taken from a line that crosses the spray plume number 3 in the radial direction. Figure 11 aims to capture the interaction between the spray plumes 2 and 3, with a line crossing the plume center of each of them.

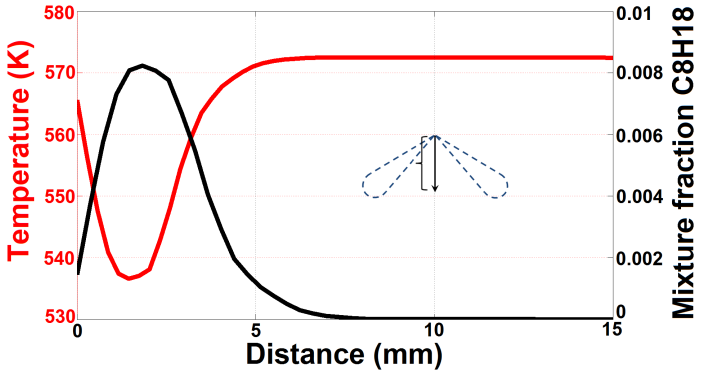

Figure 9: Temperature (red) and Iso-octane mixture fraction (black) at 0.6 ms (II)

Along the spray plume 3, one can observe that gaseous iso-octane is more poorly concentrated at the spray plume frontier with the gas phase than in comparison with the middle of

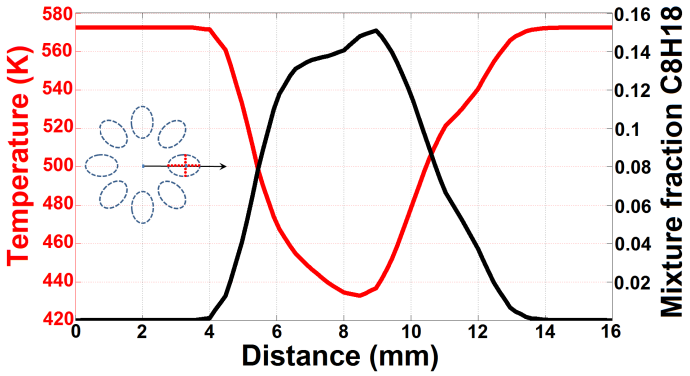

Figure 10: Temperature (red) and Iso-octane mixture fraction (black) at 0.6 ms (III)

the jet, where it reaches the maximum. The interaction between spray plumes 2 and 3 is shown from a probe line crossing both of them in a direction nearly perpendicular to the full cone spray radial direction. The results show two distinct shapes which are related to their respective spray jets. The first shape is related to spray plume 3 and the second to spray plume 2. At 0.6 ms both spray plumes present the highest iso-octane mixture fractions in regions between jet center and jet frontier, with a slight decrease at the jet center.

A mesh sensitivity study was carried out to investigate the influence of the grid size in the spray simulations. For this, the same case was run with coarser grids of 0.75 mm and 1 mm grid sizes. Figure 12 presents the penetration curves for each one of the cases, showing that with coarser grid the jet penetration is the shortest. Figure 13 shows a visualization comparing the penetration length difference in the case with grid size 0.75 mm and with grid size 0.5 mm at 0.6 ms ASOI.

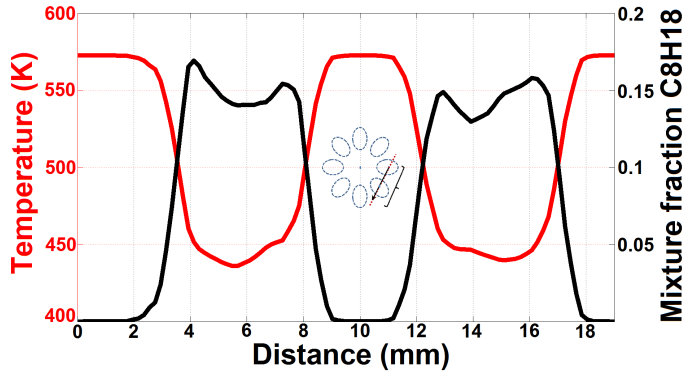

Figure 11: Temperature (red) and Iso-octane mixture fraction (black) at 0.6 ms (IV)

For reasons explained before, all cases under predict the penetration length of the experiment during the initial moments. The case with 0.5 mm grid (red) gets closer to the experimental value just after 0.4 ms and after 0.6 ms starts to over predict it slightly. The case with 0.75 mm grid reaches the experiment curve only at the end of injection at 0.78 ms, slightly over predicting it after 1 ms. The coarsest case (1mm) under predicts the penetration length over the entire simulation duration.

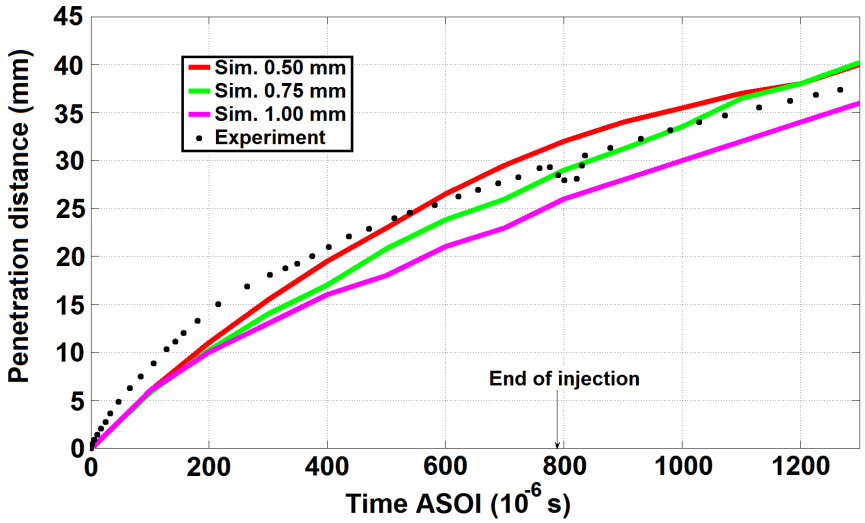

Figure 12: Mesh sensitivity study and comparison

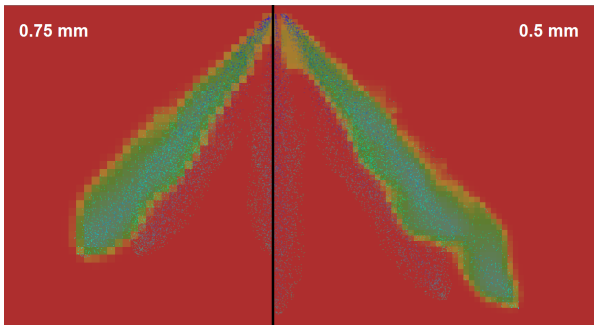

Figure 13: Effect of different grid resolution on the penetration length at 0.6 ms ASOI

4 CONCLUSIONS

Fuel-spray injection and related phenomena (exchange of momentum, heat exchange and evaporation) were simulated using Lagrangian particle tracking and large-eddy simulation with OpenFOAM-2.3.x. For this, the test-case Spray G provided by the Engine Combustion Network has been taken and used for the validation of the penetration length obtained by our LES-sprays simulations. The penetration length obtained by simulations showed good agreement with the experiment. However, for future simulations, the non-uniform concentration of particles within the spray cone should be considered, which was found out to have an impact on the penetration length. The Reitz-Diwakar model was used to represent the breakup of particles and the Rosin-Rammler CDF was employed to obtain the size distribution. Furthermore, a mesh sensitivity study was carried out in order to assess the effect of grid resolution on spray simulations, showing that the coarser the grid is, the less deep the jet penetrates.

ACKNOWLEDGEMENTS

The authors acknowledge the financial support by ThyssenKrupp within the Incentive Program to Scientific Qualification. Furthermore, we would like to thank the Center for Computational Sciences and Simulation (CCSS) of the University of Duisburg-Essen for providing the computational resources.

REFERENCES

Baumgarten, C., 2005. *Mixture Formation in Internal Combustion Engines*. Springer.

Dent, J. C., 1971. A Basis for the Comparison of Various Experimental Methods for Studying Spray Penetration. *SAE Technical Paper*, no. 710571.

ECN, 2015. Spray G operation conditions. URL: `http://www.sandia.gov/ecn/G/targetCondition/sprayG.php`.

Goryntsev, D, Sadiki, A, Klein, M, & Janicka, J, 2010. Analysis of cyclic variations of liquid fuel-air mixing processes in a realistic DISI IC-engine using Large Eddy Simulation. *International Journal of Heat and Fluid Flow*, vol. 31, pp. 845–849.

Heywood, J., 1988. *Internal Combustion Engine Fundamentals*. McGraw-Hill, Inc.

Hiroyasu, H & Arai, M, 1990. Structures of Fuel Sprays in Diesel Engines. *SAE Technical Paper*, no. 900475.

Jangi, M, Solsjo, R, Johansson, B, & Bai, X, 2015. On large eddy simulation of diesel spray for internal combustion engines. *International Journal of Heat and Fluid Flow*, vol. 53, pp. 68–80.

Karavalakis, G., Short, D., Vu, D., Russell, R. L., Asa-Awuku, A., Jung, H., Johnson, K. C., & Durbin, T. D., 2015. The impact of ethanol and iso-butanol blends on gaseous and particulate emissions from two passenger cars equipped with spray-guided and wall-guided direct injection SI (sparkignition engines. *Energy*, vol. 82, pp. 168–179.

Kim, N., Cho, S., & Min, K., 2015. A study on the combustion and emission characteristics of an SI engine under full load conditions with ethanol port injection and gasoline direct injection. *Fuel*, vol. 158, pp. 725–732.

Liu, H., Wang, Z., & Wang, J., 2015. Methanol-gasoline DFSI (dual-fuel spark ignition) combustion with dual-injection for engine knock suppression. *Energy*, vol. 73, pp. 686–693.

Liu, H., Wang, Z., Long, Y., Xiang, S., Wang, J., & Wagnon, S. W., 2015. Methanol-gasoline Dual-fuel Spark Ignition (DFSI) combustion with dual-injection for engine particle number (PN) reduction and fuel economy improvement. *Energy*. DOI: `10.1016/j.energy.2015.06.051`.

Lucchini, T, D'Errico, G, & Ettorre, D, 2011. Numerical investigation of the spray-mesh-turbulence interactions for high-pressure, evaporating sprays at engine conditions. *International Journal of Heat and Fluid Flow*, vol. 32, pp. 285–297.

Maricq, M. M., Szente, J. J., & Jahr, K., 2012. The Impact of Ethanol Fuel Blends on PM Emissions from a Light-Duty GDI Vehicle. *Aerosol Science and Technology*, vol. 46, pp. 576–583.

Marshall, W. R. & Ranz, W. E., 1952. *Internal Combustion Engine Modeling*. Hemisphere Publishing.

Reitz, R. D. & Bracco, F. V., 1986. *The Encyclopedia of Fluid Mechanics*. Gulf Publishing.

Subramaniam, S., 2013. Lagrangian-Eulerian methods for multiphase flows. *Progress in Energy and Combustion Science*, vol. 39, pp. 215–245.

The International Council on Clean Transportation, 2014. EU CO2 Emission Standards for Passenger Cars and Light-comercial vehicles. In: Berlin.

Vuorinen, V. A., Hillamo, H, Kaario, O, Nuutinen, M, Larmi, M, & Fuchs, L, 2011. Effect of Droplet Size and Atomization on Spray Formation: A Priori Study Using Large-Eddy Simulation. *Flow Turbulence Combust*, vol. 86, pp. 533–561.

Wierzba, A, 1990. Deformation and breakup of liquid drops in a gas stream at nearly critical Weber numbers. *Experiments in Fluids*, vol. 9, pp. 59–64.

Yang, J. L. & Anderson, R. W., 1998. Fuel Injection Strategies to Increase Full-Load Torque Output of a Direct-injection SI Engine. *SAE Technical Paper*, no. 980495.

Zheng, Z., Tian, X., & Zhang, X., 2015. Effects of split injection proportion and the second injection time on the mixture formation in a GDI engine under catalyst heating mode using stratified charge strategy. *Applied Thermal Engineering*, vol. 84, pp. 237–245.